Check for updates

Development of ice-shelf estuaries promotes fractures and calving

Alexandra L. Boghosian [1,2 ✉], Lincoln H. Pitcher [3,4], Laurence C. Smith[4,5], Elena Kosh[6], Patrick M. Alexander[1,7], Marco Tedesco[1,7,8,9] and Robin E. Bell[1]

As the global climate warms, increased surface meltwater production on ice shelves may trigger ice-shelf collapse and enhance global sea-level rise. The formation of surface rivers could help prevent ice-shelf collapse if they can efficiently evacuate meltwater. Here we present observations of the evolution of a surface river into an ice-shelf estuary atop the Petermann Ice Shelf in northwest Greenland and identify a second estuary at the nearby Ryder Ice Shelf. This surface-hydrology process can foster fracturing and enhance calving. At the Petermann estuary, sea ice was observed converging at the river mouth upstream, indicating a flow reversal. Seawater persists in the estuary after the surrounding icescape is frozen. Along the base of Petermann estuary, linear fractures were initiated at the calving front and propagated upstream along the channel. Similar fractures along estuary channels shaped past large rectilinear calving events at the Petermann and Ryder ice shelves. Increased surface melting in a warming world will enhance fluvial incision, promoting estuary development and longitudinal fracturing orthogonal to ice-shelf fronts, and increase rectilinear calving. Estuaries could develop in Antarctica within the next half-century, resulting in increased calving and accelerating both ice loss and global sea-level rise.

Ice shelves are increasingly losing mass[1] due to both widespread basal melting and calving[2] and are also vulnerable to rapid collapse triggered by surface hydrology[3]. Ice-shelf surface hydrology can lead to rapid ice-shelf collapse through the formation of surface ponds, which weaken and break the ice shelf through flexure[4,5] and hydrofracture[6]. However, recent observations of ice-shelf rivers suggest that water export off the ice shelf may limit the damage potential of ice-shelf surface hydrology[7]. The impact that rivers have on ice-shelf stability remains unresolved[8,9]. A recent coupled ice-sheet–climate model of Antarctica assumes that meltwater remains static and has predicted that Antarctica contributes one metre to global average sea-level rise by 2100 (ref. [10]). However, satellite observations show widespread water transport onto Antarctica's ice shelves[7] and large volumes of water transport across Greenland[11]. Ice-shelf rivers form in response to climate and albedo characteristics that drive meltwater production[7,12] and ocean conditions that create linear depressions in ice-shelf surface topography[13,14] where ice-shelf rivers can flow[9]. As global temperatures rise, more ice-shelf rivers will develop, increasing the urgency to understand the impact of surface hydrology on ice-shelf stability.

The Petermann Ice Shelf in northwest Greenland (Fig. 1), one of three remaining large ice shelves in Greenland[15], flows along an ~25-km-wide fjord. The ice-shelf surface supports a system of lakes and rivers first observed in 1978 (refs. [16,17]). This system may serve as an analogue for the future of Antarctica's ice shelves. Like the Nansen river in East Antarctica[8], the Petermann river flows to the ocean[8,16], terminating at the ice-shelf edge (Fig. 1a) that was formed by the last major calving event in 2012 (ref. [15]). Climatology-forced regional climate models show that surface melting persists on the Petermann Ice Shelf for ~80 days each year (Extended Data Fig. 1). Rivers and lakes develop on bare ice that is exposed on the ice shelf, a region of low accumulation (Extended Data Fig. 2). The Petermann river[8] flows along a linear depression in the centre of the ice shelf, which is the surface expression of a 1–2-km-wide basal channel[14]. Focused ocean melting initiates this channel within ~5 km of the grounding line, carving 200–400 m upward into the ice-shelf base[14]. The resulting linear depression is a persistent feature of the ice-shelf surface[18]. The Nansen river also flows atop a basal channel[9]. Through this imprint on ice-shelf morphology, ocean processes control the location of ice-shelf rivers.

Observations of ice-shelf estuaries

Estuaries form near river mouths, where fresh fluvial waters and saline ocean waters mix[19], but had not been identified on ice shelves. Using high-resolution satellite and aerial imagery, we observed an ice-shelf estuary at the calving front of the Petermann Ice Shelf where the Petermann river directly connects to the ocean (Fig. 1). Four observations indicate the existence of the Petermann estuary: the presence of sea ice in the lower reach of the river (<1 km from the terminus; Fig. 1a,b); the presence of water in the lower reach of the river channel after the end of the melt season (Fig. 1c and Extended Data Fig. 1); the fan-shaped convergence of sea ice at the river mouth (Fig. 1a,b); and the widening of the channel within 1 km of the terminus (Extended Data Figs. 2b and 3). Floating ice with the same shape and texture as offshore sea ice indicates that seawater is present in the channel (Fig. 1a,b) as far as 460 m upstream from the river mouth (Fig. 1a,b). Seawater in the channel is also identified in imagery collected 26 days after the melt season (on 12 September 2014; Fig. 1c and Extended Data Fig. 1) when surface lakes are frozen and the adjacent ice-shelf surface is dry, meaning that the ocean is the
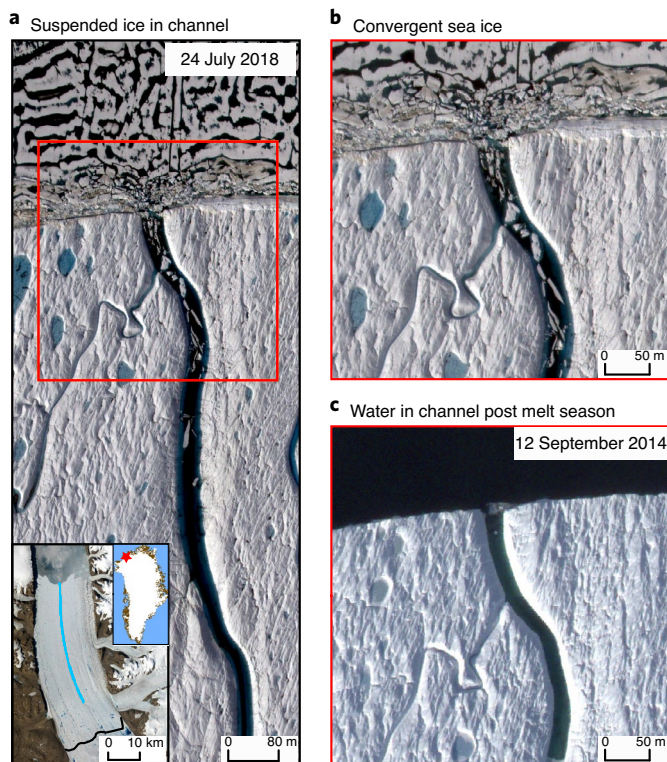
Fig. 1 | Evidence for the Petermann estuary. a, Suspended sea ice in the lower reach of the Petermann river and convergent sea ice at the mouth of the Petermann estuary in a WorldView-2 image collected 24 July 2018. The red box denotes the extent of **b** and **c**. Inset shows a Landsat 8 image of the Petermann Ice Shelf collected on 11 July 2016 with a map of Greenland in the upper right and the location of the Petermann Ice Shelf marked with a red star. Blue line denotes the Petermann river extent. Black line approximates the 2008 grounding line[38]. **b**, Detail of the image shown in **a**. The convergence of sea ice at the mouth of the estuary and suspended sea ice in the channel indicate a flow reversal. **c**, Ocean water atop the ice shelf after the end of the melt season, on 12 September 2014. Credit: **a,b**, (2018) DigitalGlobe, Inc.; **c**, (2014) DigitalGlobe Inc.

only source of liquid water. Seawater persisted in the channel after the melt season in September 2013–2016 (Extended Data Fig. 1). Flow reversal at the estuary is confirmed by the distinctive pattern of convergent sea ice at the estuary mouth (Fig. 1a,b) and is probably a result of tidal and/or baroclinic exchange flow[19]. We also find that river widths tripled in the estuary between 2010 and 2018 (Extended Data Figs. 2 and 3), while upstream (>2 km from the terminus) widths remained stable (Extended Data Fig. 3). This downstream widening is consistent with the establishment of an estuary. Once a river channel reaches sea level, it cannot incise downward any further. There is relatively little flow gradient to drive velocity, so more kinetic energy in the system is dissipated by melting channel walls. Melting and widening is also enhanced by the presence of relatively warm (>0 °C)[20] ocean water in the estuary. These observations indicate that the Petermann estuary currently reaches at least 0.5 km upstream from the ice-shelf front. Ice-shelf estuaries have formed on the Ryder Ice Shelf in Greenland, evidenced in 2019 by dark water at the mouth of the channel and a continuous water surface between the river mouth and the ocean (Fig. 2c), and in 2014 by seawater in the channel after the melt season (Extended Data Fig. 4).

Longitudinal fracture development and rectilinear calving

After the Petermann river evolves to an estuary, new ice-shelf fractures form at the calving front and propagate upstream along the channel, parallel to ice flow (Fig. 2a,b and Extended Data Fig. 5). The fractures are located in the centre of the river channel and appear as dark linear features in satellite images (Fig. 2a and Extended Data Fig. 5) and aerial photographs (Fig. 2b,c). These features could be interpreted as the deposition of cryoconite; however, sediments are unlikely to accumulate in the channel centre where water velocity is high. The ~90-m-long fracture first appeared along the channel bottom at the mouth of the river in 2014, a minimum of 2 years after the estuary formed (Methods) (Fig. 2a). By 2017, longitudinal fractures extended ~1.6 km upstream from the ice-shelf front, within the estuary's reach (Fig. 2a and Extended Data Fig. 3a). Aerial photographs of the fractures show a dark water colour similar to through-cutting rifts (Fig. 2b), indicating that the fractures propagate through the ice shelf. The Ryder Ice Shelf has similar longitudinal fractures along the bottom of its estuary (Fig. 2c). Longitudinal fractures discovered and initiated at estuary mouths are notably absent in upstream reaches of ice-shelf rivers where estuarine processes are not active.

While many calving events on the Petermann Ice Shelf formed from transverse fractures perpendicular to flow[21], since 1978 at least two rectilinear calving events have formed along a longitudinal river (Fig. 3a). An early aerial image of the Petermann Ice Shelf collected in 1978 shows a linear river transporting surface melt across the shelf (Fig. 3a). By 1999, calving events had fractured along the 1978 river (Fig. 3a). The river again terminated in the ocean, potentially forming an estuary. In 2008, a ~10-km-long linear fracture formed along the 1999 river channel (Fig. 3a), creating another rectilinear calving event (Fig. 2a). Similar rectilinear calving occurred along a surface river and associated estuary on the Ryder Ice Shelf (Fig. 3b), where calving events typically span the full ice-shelf width. Longitudinal fractures are not initiated in upstream reaches of either river. We assign the term 'estuarine weakening' to the propagation of longitudinal fractures along the ice-shelf river and estuary systems producing distinctive rectilinear calving geometries (Fig. 3c). While previous work has suggested that ice-shelf rivers enhance transverse fractures[9], estuaries on the Petermann and Ryder ice shelves appear to have contributed to the formation of longitudinal fractures and rectilinear calving events over at least the past three decades.

Implications of estuary formation on calving

Based on observations of the Petermann and Nansen rivers[8,9], we suggest that ice-shelf estuaries evolve from surface rivers that incise atop basal channels given sufficient surface meltwater production. The Nansen river and the upper reaches of the Petermann river represent the river phase of this evolution. During this phase, the river's location is fixed by pre-existing surface depressions controlled by basal channels[9] and the river incises into the same ice each year while exporting water off the ice shelf via waterfalls[8]. There are no direct feedbacks between the ice-shelf surface hydrology and the ocean and no channel-parallel fractures develop. Transverse fractures may be enhanced during the river phase[9]. The estuary phase begins when an ice-shelf river incises to sea level. Observations indicate that this requires consistent river incision during long melt seasons. The Nansen river, which has not become an estuary, does not form annually and only persists for 5–25 days each year[8]. In contrast, the Petermann river has formed annually since 2010 and flows for 59 days each year on average (Methods). The Petermann river incised to sea level between 2010 and 2013 at a rate ranging from 1 to 5.5 cm d^{−1}, overlapping the 3–10 cm d^{−1} incision range measured on glaciers and ice sheets[22] (Methods). During the estuary phase, a direct connection to the ocean is established, leading to new processes at the ice-shelf front, including the advance of relatively warm ocean water onto the ice-shelf surface, flow reversal in the channel and the presence of water on the ice-shelf surface after the melt season. During the estuary phase, longitudinal fractures form at the front of the ice shelf and propagate upstream. We hypothesize
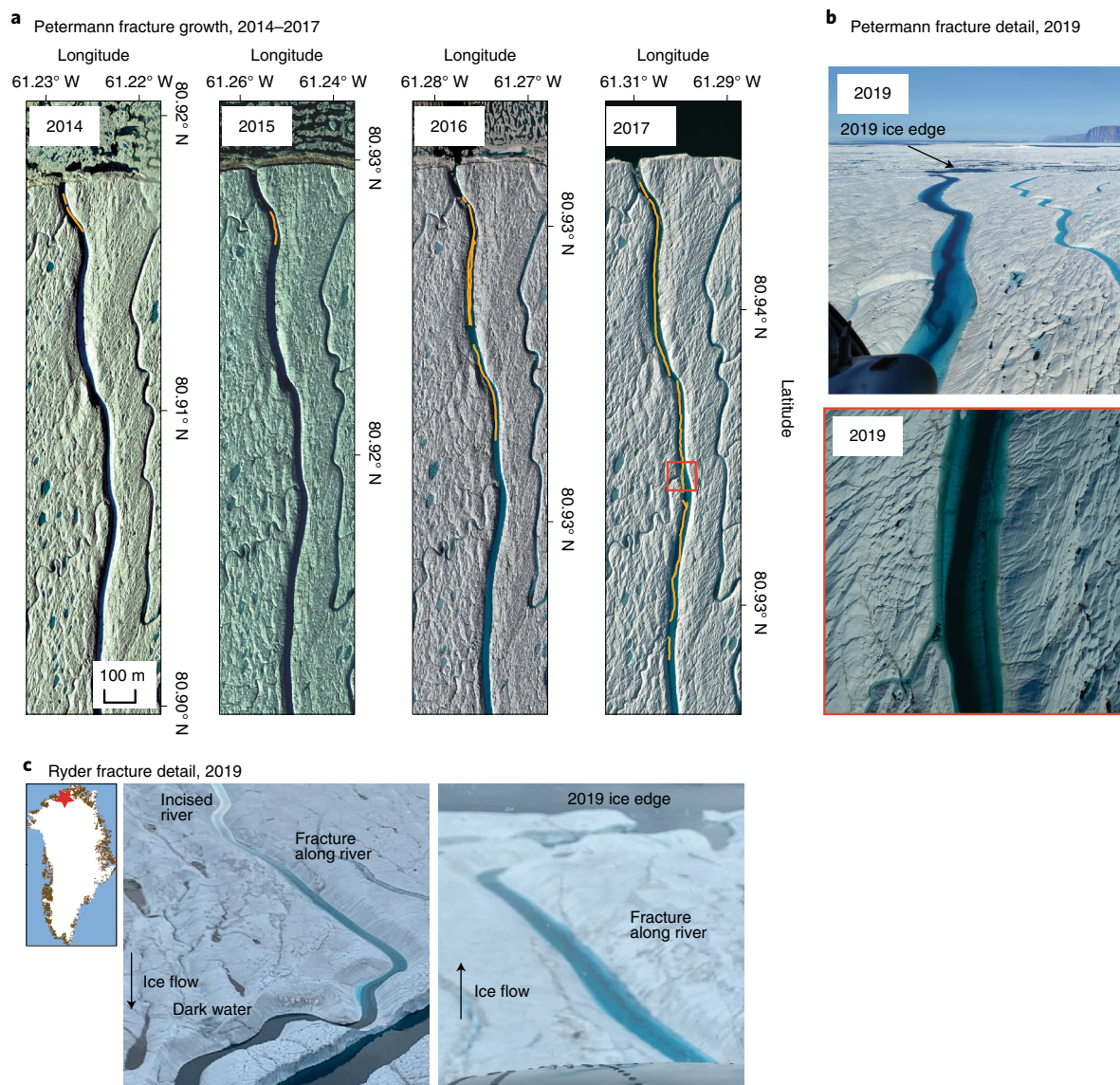
Fig. 2 | Development of longitudinal fracture along the Petermann and Ryder ice-shelf rivers. a, From left to right, the growth of longitudinal fractures (gold line) in the Petermann estuary from 2014 to 2017. Images were collected on 14 July 2014, 17 July 2015, 15 July 2016 and 25 July 2017 (WorldView). Undigitized versions of these figures are included in Extended Data Fig. 5. **b**, Aerial images of the fracture at the bottom of the Petermann river channel. Top image collected on 27 July 2019; bottom image collected on 15 July 2019. Red box in **a** shows the approximate locations of **b**. **c**, Aerial images of the river, estuary and fractures on the Ryder Ice Shelf (location map on upper left). Left: an incised river channel with dark water at the ice-shelf front indicates incision to sea level and the presence of an estuary at the river mouth. Dark line initiated at the ice-shelf front indicates a longitudinal fracture along the river. Right: aerial view of fracturing at the bottom of the river on the Ryder Ice Shelf. Images collected on 8 November 2019 and 13 October 2019. Credit: **a**, (2014, 2015, 2016, 2017) DigitalGlobe, Inc.; **b**, Roger Fishman; **c**, Josh Willis.

that the evolution of an ice-shelf river to an estuary promotes fractures orthogonal to the calving front and eventual rectilinear calving events.

As opposed to ice-shelf collapse triggered by warming climate and surface melting[23], calving of tabular icebergs is understood to be controlled by ice-shelf dynamics and structure[24], independent of climatic conditions. However, the estuary-induced fractures along the Petermann and Ryder estuaries, along with the history of rectilinear calving along rivers, indicate that surface hydrology, driven by climatic conditions, may play a role in iceberg calving. The fractures form at the ice-shelf front, downstream of the compressive arch where ice-shelf stresses are otherwise isotropic[25] (Fig. 3c). We suggest estuary formation may have localized stresses at the ice-shelf front through both enhanced incision and loading

(Fig. 3). At the Petermann estuary, relatively warm ocean water[20] advancing into the river channel may locally thin and weaken the ice through enhanced channel incision. As flow reversal limits water export, increased water storage on the shelf will lead to increased loading. Periodic loading would also increase at the ice-shelf front when ocean water is present at the mouth of the estuary after the end of the melt season. We consider the possibility that the fractures resulted from stress concentrated by the basal channel[26] and/or the ice shelf's progressive detachment from the fjord walls downstream[27], which would cause extensional stresses to exist transverse to the direction of flow. However, on the Nansen Ice Shelf, extensional stress transverse to the basal channel and river system was found insufficient to initiate longitudinal fractures[9]. We speculate that the development of estuaries may increase rectilinear

a Petermann rivers and rectilinear calving, 1978–2008
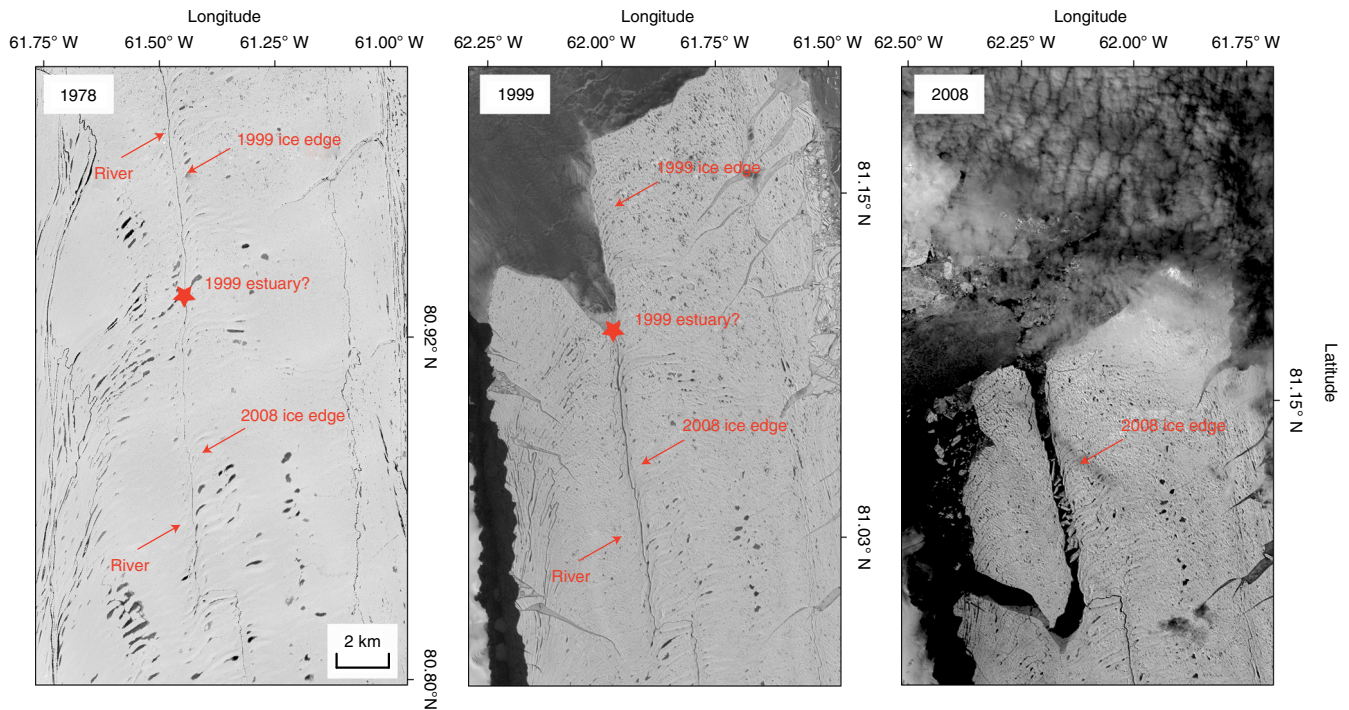
b Ryder rivers and rectilinear calving, 2010–2014
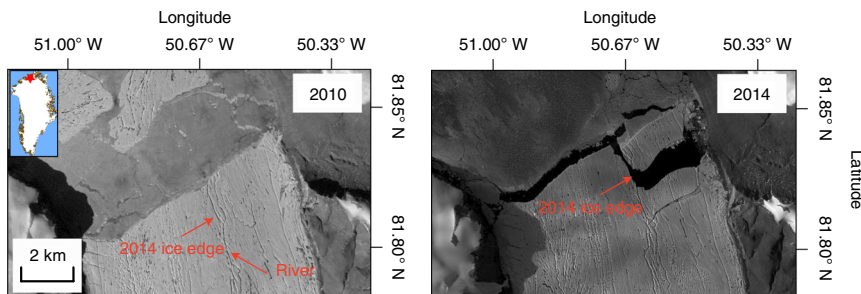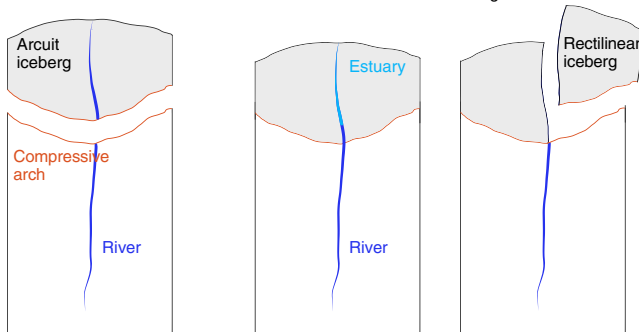

c Estuarine weakening

Fig. 3 | Rectilinear calving and estuarine weakening at the Petermann and Ryder ice shelves. a, Left: in 1978, a long, straight river was present on the Petermann Ice Shelf. Future ice edges (1999 and 2008) and estuaries (1999) are annotated in red (image from 3 July 1978). Middle: in 1999, the ice shelf had calved along the upper portion of the 1978 river, with the lower portion reaching the ocean in a possible estuary (red star); 2008 ice edge annotated in red (7 July 1999 panchromatic Landsat 7 image). Right: image from 2008 shows that calving occurred along the 1999 river also visible in 1978; the iceberg produced by the longitudinal fracture coincident with the river is present (13 July 2008 panchromatic Landsat 7 image). **b**, Left: in 2010, an ice-shelf-terminating river was present on the east side of the Ryder Ice Shelf (location map in upper left). The calving-front morphology was straight along the width of the shelf. Future 2014 ice edge is annotated in red (8 July 2010 panchromatic Landsat 7 image). Right: in 2014, the ice shelf had calved along the upper portion of the 2010 river (1 August 2014 panchromatic Landsat 7 image). **c**, Schematic of estuarine weakening processes with shaded compressive arch. Longitudinal fractures are initiated at the estuary mouth, downstream of the compressive arch (grey shaded region).
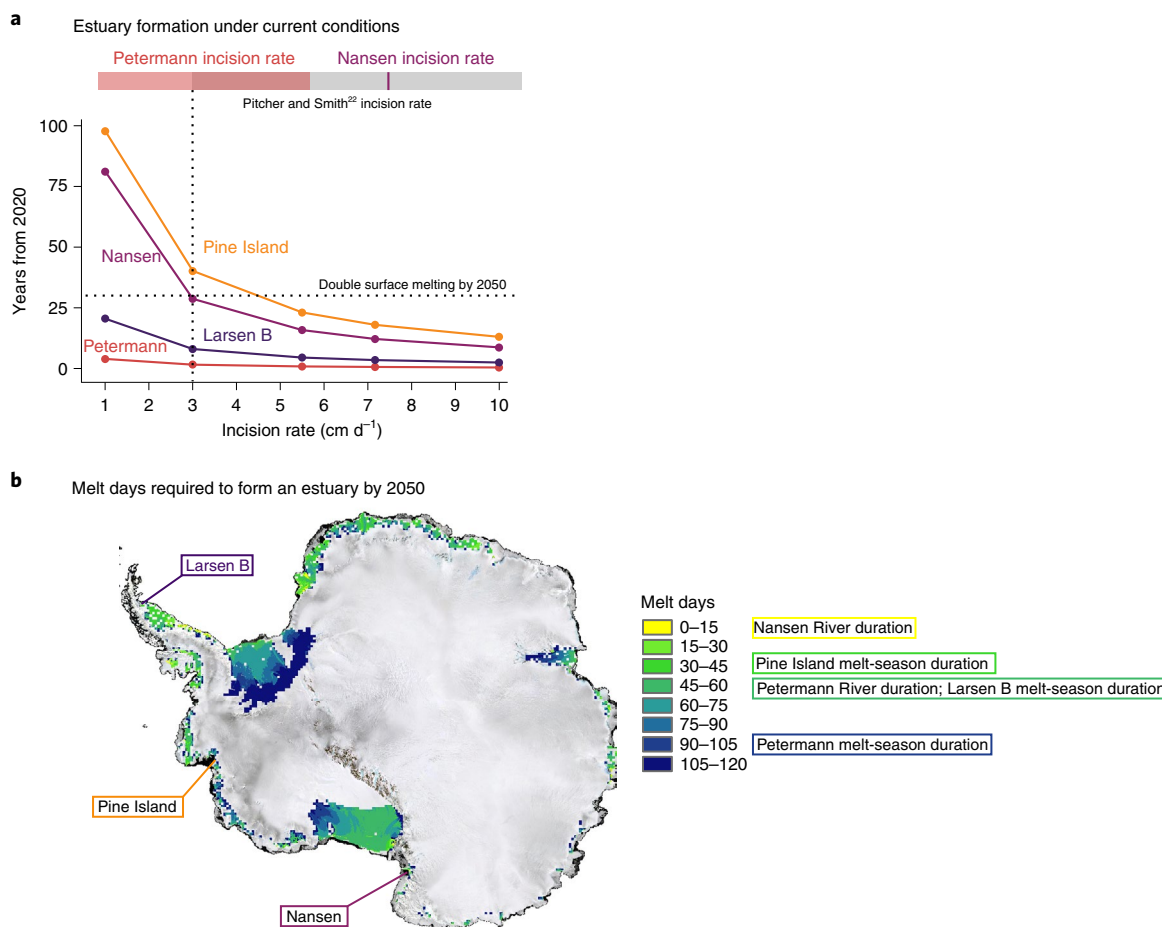
Fig. 4 | Estuary formation in Antarctica. a, Predictions of time (years) until an estuary forms on ice shelves as a function of incision rate. Estimates are provided for the Nansen and Pine Island ice shelves, as well as the Petermann and Larsen B ice shelves. The horizontal dashed line marks 30 years from the present, 2050, when Antarctic surface melt is expected to double. The vertical dashed line shows the conservative estimate of incision rate of 3 cm d⁻¹ (ref. [22]) chosen to report estuary formation predictions and used in subsequent calculations (Methods). The horizontal red bar indicates the range of incision rates estimated for the Petermann River (Methods) and the horizontal grey bar indicates the range of incision rates reported for supraglacial rivers and streams on grounded ice[22]. The purple line marks the incision rate estimated for the Nansen river (Methods). **b**, Length of the melt season necessary to produce estuaries on Antarctic ice shelves in 30 years (by 2050).

calving and posit estuarine weakening as a climate-driven calving mode. Further studies including direct measurements and modelling of estuary evolution will provide insights into how longitudinal fractures form and influence ice shelves.

Potential estuary formation in a warming world

As the global climate warms, surface melting on Antarctica's ice shelves will double in the next 30 years[12] and probably form more rivers atop basal channels[8]. Linear topographic depressions, associated with basal channels, have been identified across Antarctica[9,28]. Should sufficient surface meltwater form, we predict that these depressions would organize meltwater into rivers and set the stage for estuary development. We develop a first-order model of estuary evolution and apply it to ice shelves where basal channels and rivers have been documented[8,9,13,29]. Using a range of incision rates, we forecast how long it would to take to form estuaries under current conditions, that is, the length of the Antarctic melt season remains the same (Methods). These estimates assume that the ice surface is free of firn, permitting open-channel flow, as is observed on the Petermann Ice Shelf. Using the current melt-season duration[30,31], observations of rivers[8,29], a conservative estimate of river incision[22] of 3 cm d⁻¹, ice-shelf elevation[8,32,33] and ice-shelf elevation change[1,34]

(Extended Data Table 1), we estimate that an estuary could form in 40 years on the Pine Island Ice Shelf and in 29 years on the Nansen Ice Shelf (Fig. 4a and Methods). While meltwater ponding drove the collapse of the Larsen B Ice Shelf[3,23], as waterfalls were observed[35] on the ice shelf and surface streams terminated in rifts[29], estuaries may have developed. For Larsen B, only a decade of incision would have been required for estuaries and possibly fractures to form (Fig. 4a and Methods). This estuarine weakening through rectilinear fractures could have introduced additional weaknesses in the ice shelf before its collapse was triggered by lake drainage. These predictions are sensitive to incision rate (Fig. 4a), which will vary with surface meltwater production, and depend on the presence of firn, which modulates the efficiency of a river to drain surface melt. The greatest uncertainty in predicting estuary formation is the large range of incision rates used in our calculations due to the lack of in situ observations (Methods).

Given the projections of surface melt increase in Antarctica[12], we also estimate the melt-season duration required for Antarctic supraglacial rivers to evolve into estuaries in 30 years (Methods). We use our estuary evolution model constrained by measurements of ice-shelf elevation[33], ice-shelf elevation change[1] and a conservative incision rate[22] of 3 cm d⁻¹ (Methods). Again, we neglect the role

of firn hydrologic processes and assume open-channel flow over a firn-free, bare ice surface. As the climate warms in Antarctica, low permeability surfaces will expand as they have in Greenland[36], promoting surface meltwater runoff and open-channel flow. In this forecast, Antarctic rivers would have to incise at the ice-shelf front for 30–45 days each season for 3 decades to produce estuaries (Fig. 4b). This melt-season duration is up to 1.5 times the average number of observed annual melt days on Antarctic ice shelves from 1978 to 2004 (ref. [37]). If the melt season lengthens to the conditions that produced the collapse of the Larsen B Ice Shelf, 45–60-days, estuaries would be widespread but restricted to the outer portions of the large ice shelves (Amery, Filcher-Ronne and western Ross). When the Antarctic melt season lengthens to the current ~80 days at the Petermann Ice Shelf, most Antarctic ice-shelf rivers would incise to estuaries within 3 decades (Fig. 4b). Establishing an accurate chronology of the onset of estuarine weakening will benefit from direct measurements of ice-shelf rivers, as well as an understanding of the evolution of firn and other ice-shelf surface processes.

Multiple observations of ice-shelf estuaries extend our view of ice-shelf surface hydrology and stability beyond a simplified lakes–rivers framework. We suggest that the role that rivers play in ice-shelf stability depends on whether the river terminates in a waterfall or evolves into an estuary. As long as water is removed off the shelf through a waterfall, rivers may mitigate ice-shelf instability driven by surface lakes. As rivers evolve to ice-shelf estuaries, new ice/ocean processes are introduced to the ice-shelf front that can concentrate stress and favour a rectilinear calving mode. We advance estuarine weakening as a new process that may enhance ice-shelf fracture and calving, linked to both atmospheric trends and patterns that drive surface melt and to ocean melting that forms ice-shelf basal channels. As rivers and streams are found on many Antarctic ice shelves[7], it is possible that the formation of ice-shelf estuaries is already underway. Our first-order estimates of estuary formation in Antarctica indicate estuaries may form within the next 30 years, assuming that Antarctica's future surface resembles that of present-day Greenland. If ice-shelf estuaries form in Antarctica, we speculate that calving may increase due to the introduction of estuarine weakening promoting rectilinear calving. Estimates of estuary evolution in Antarctica would be improved by detailed analysis of ice-shelf surface processes, including firn hydrology. The discovery of the Petermann and Ryder estuary systems emphasizes the need for further investigation of how ice-shelf rivers evolve and impact ice-shelf stress, so that that a more complete set of ice-shelf surface hydrologic processes can be included in models and predictions of ice-sheet stability.

Online content

References

1. Paolo, F. S., Fricker, H. A. & Padman, L. Volume loss from Antarctic ice shelves is accelerating. *Science* **348**, 327–331 (2015).
2. Rignot, E., Jacobs, S., Mouginot, J. & Scheuchl, B. Ice-shelf melting around Antarctica. *Science* **341**, 266–270 (2013).
3. Banwell, A. F., MacAyeal, D. R. & Sergienko, O. V. Breakup of the Larsen B Ice Shelf triggered by chain reaction drainage of supraglacial lakes. *Geophys. Res. Lett.* **40**, 5872–5876 (2013).
4. Banwell, A. F. & MacAyeal, D. R. Ice-shelf fracture due to viscoelastic flexure stress induced by fill/drain cycles of supraglacial lakes. *Antarct. Sci.* **27**, 587–597 (2015).
5. MacAyeal, D. R., Sergienko, O. V. & Banwell, A. F. A model of viscoelastic ice-shelf flexure. *J. Glaciol.* **61**, 635–645 (2015).
6. Scambos, T. et al. Ice shelf disintegration by plate bending and hydro-fracture: satellite observations and model results of the 2008 Wilkins Ice Shelf break-ups. *Earth Planet. Sci. Lett.* **280**, 51–60 (2009).
7. Kingslake, J., Ely, J. C., Das, I. & Bell, R. E. Widespread movement of meltwater onto and across Antarctic ice shelves. *Nature* **544**, 349–352 (2017).
8. Bell, R. E. et al. Antarctic ice shelf potentially stabilized by export of meltwater in surface river. *Nature* **544**, 344–348 (2017).
9. Dow, C. F. et al. Basal channels drive active surface hydrology and transverse ice shelf fracture. *Sci. Adv.* **4**, eaao7212 (2018).
10. DeConto, R. M. & Pollard, D. Contribution of Antarctica to past and future sea-level rise. *Nature* **531**, 591–597 (2016).
11. Smith, L. C. et al. Efficient meltwater drainage through supraglacial streams and rivers on the southwest Greenland ice sheet. *Proc. Natl Acad. Sci. USA* **112**, 1001–1006 (2015).
12. Trusel, L. D. et al. Divergent trajectories of Antarctic surface melt under two twenty-first-century climate scenarios. *Nat. Geosci.* **8**, 927–932 (2015).
13. Dutrieux, P. et al. Basal terraces on melting ice shelves. *Geophys. Res. Lett.* **41**, 5506–5513 (2014).
14. Rignot, E. & Steffen, K. Channelized bottom melting and stability of floating ice shelves. *Geophys. Res. Lett.* **35**, L02503 (2008).
15. Hill, E. A., Carr, J. R. & Stokes, C. R. A review of recent changes in major marine-terminating outlet glaciers in northern Greenland. *Front. Earth Sci.* **4**, 111 (2017).
16. Macdonald, G. J., Banwell, A. F. & MacAyeal, D. R. Seasonal evolution of supraglacial lakes on a floating ice tongue, Petermann Glacier, Greenland. *Ann. Glaciol.* **59**, 56–65 (2018).
17. Korsgaard, N. J. et al. Digital elevation model and orthophotographs of Greenland based on aerial photographs from 1978–1987. *Sci. Data* **3**, 160032 (2016).
18. Münchow, A., Padman, L. & Fricker, H. A. Interannual changes of the floating ice shelf of Petermann Gletscher, north Greenland, from 2000 to 2012. *J. Glaciol.* **60**, 489–499 (2014).
19. Holland, P. G. et al. in *Encyclopedia of Hydrology and Water Resources* (ed. Herschy, W. R.) 244–248 (Springer, 1998).
20. Johnson, H. L., Münchow, A., Falkner, K. K. & Melling, H. Ocean circulation and properties in Petermann Fjord, Greenland. *J. Geophys. Res. Oceans* **116**, C01003 (2011).
21. Hill, E. A., Carr, J. R., Stokes, C. R. & Gudmundsson, G. H. Dynamic changes in outlet glaciers in northern Greenland from 1948 to 2015. *Cryosphere* **12**, 3243–3263 (2018).
22. Pitcher, L. H. & Smith, L. C. Supraglacial streams and rivers. *Annu. Rev. Earth Planet. Sci.* **47**, 421–452 (2019).
23. Scambos, T. A., Hulbe, C. & Fahnestock, M. in *Antarctic Peninsula Climate Variability: Historical and Paleoenvironmental Perspectives* (eds Domack, E. et al.) 79–92 (American Geophysical Union, 2003).
24. Lazzara, M. A., Jezek, K. C., Scambos, T. A., MacAyeal, D. R. & van der Veen, C. J. On the recent calving of icebergs from the Ross Ice Shelf. *Polar Geogr.* **23**, 201–212 (1999).
25. Doake, C. S. M., Corr, H. F. J., Rott, H., Skvarca, P. & Young, N. W. Breakup and conditions for stability of the northern Larsen Ice Shelf, Antarctica. *Nature* **391**, 778–780 (1998).
26. Bassis, J. N. & Ma, Y. Evolution of basal crevasses links ice shelf stability to ocean forcing. *Earth Planet. Sci. Lett.* **409**, 203–211 (2015).
27. Hill, E. A., Gudmundsson, G. H., Carr, J. R. & Stokes, C. R. Velocity response of Petermann Glacier, northwest Greenland, to past and future calving events. *Cryosphere* **12**, 3907–3921 (2018).
28. Alley, K. E., Scambos, T. A., Siegfried, M. R. & Fricker, H. A. Impacts of warm water on Antarctic ice shelf stability through basal channel formation. *Nat. Geosci.* **9**, 290–293 (2016).
29. Glasser, N. F. & Scambos, T. A. A structural glaciological analysis of the 2002 Larsen B ice-shelf collapse. *J. Glaciol.* **54**, 3–16 (2008).
30. Trusel, L. D., Frey, K. E., Das, S. B., Munneke, P. K. & van den Broeke, M. R. Satellite-based estimates of Antarctic surface meltwater fluxes. *Geophys. Res. Lett.* **40**, 6148–6153 (2013).
31. Scambos, T. A., Hulbe, C., Fahnestock, M. & Bohlander, J. The link between climate warming and break-up of ice shelves in the Antarctic Peninsula. *J. Glaciol.* **46**, 516–530 (2000).
32. Rack, W. & Rott, H. Pattern of retreat and disintegration of the Larsen B Ice Shelf, Antarctic Peninsula. *Ann. Glaciol.* **39**, 505–510 (2004).
33. Howat, I. M., Porter, C., Smith, B. E., Noh, M. J. & Morin, P. The reference elevation model of Antarctica. *Cryosphere* **13**, 665–674 (2019).
34. Shepherd, A., Wingham, D., Payne, T. & Skvarca, P. Larsen Ice Shelf has progressively thinned. *Science* **302**, 856–859 (2003).
35. Warm ocean explains Antarctic ice shelf collapse. *University of Cambridge* (30 October 2003); https://www.geog.cam.ac.uk/research/projects/larseniceshelf/pressrelease.pdf

36. MacFerrin, M. et al. Rapid expansion of Greenland's low-permeability ice slabs. *Nature* **573**, 403–407 (2019).

37. Liu, H., Wang, L. & Jezek, K. C. Spatiotemporal variations of snowmelt in Antarctica derived from satellite scanning multichannel microwave radiometer and Special Sensor Microwave Imager data (1978–2004). *J. Geophys. Res. Earth Surf.* **111**, F01003 (2006).

38. Bjørk, A. A., Kruse, L. M. & Michaelsen, P. B. Brief communication: Getting Greenland's glaciers right—a new data set of all official Greenlandic glacier names. *Cryosphere* **9**, 2215–2218 (2015).

Methods

Satellite imagery. We analysed 35 high-resolution images collected by the WorldView-1, WorldView-2, WorldView-3, GeoEye and QuickBird satellites (collectively, the DigitalGlobe constellation) between 2010 and 2018 to track the evolution of the estuary and longitudinal fractures (Extended Data Table 2). Except for WorldView-1, these satellites collect multispectral data at ~2 m spatial resolution. WorldView-1 collects panchromatic data at ~0.5 m. The Polar Geospatial Center (PGC) provided the orthorectified, projected and top-of-atmosphere corrected imagery.

We analysed 49 cloud-free, pan-sharpened true-colour images at 15 m resolution collected by the Landsat 8 Operational Land Imager from 2014 to 2016 to constrain the number of days that the Petermann river flowed to the ice-shelf edge (Extended Data Table 3). We use the radiometrically calibrated and orthorectified L1TP Landsat product provided by the US Geological Survey. We apply a top-of-atmosphere correction to each image using dark object subtraction in MATLAB (https://www.mathworks.com/matlabcentral/fileexchange/50636-landsat8-radiance-reflectance-brightness-temperature-and-atmospheric-correction).

We use three additional 15 m resolution panchromatic images collected by the Landsat 7 Enhanced Thematic Mapper Plus sensor and one additional panchromatic Landsat 8 image to track the rectilinear calving on the Petermann and Ryder ice shelves (Extended Data Table 3). We use the radiometrically calibrated and orthorectified L1TP Landsat product provided by the US Geological Survey and do not apply a top-of-atmosphere correction to the panchromatic images.

Aerial imagery, digital elevation models and field photography at the Petermann Ice Shelf. We use one image from the National Aeronautics and Space Administration's Operation IceBridge (OIB) Digital Mapping System (DMS)[39] camera collected in 2010 in our estuary analysis (Extended Data Table 4). DMS data have a spatial resolution of 40 cm and a vertical accuracy of 10 cm (ref. [40]). We use the DMS-derived digital elevation model (DEM) (Extended Data Table 4) to constrain the river's incision rate.

We use 2 m resolution aerial imagery collected by the Agency for Data Supply and Efficiency[17] (Extended Data Table 4) in 1978 to track rivers.

We use aerial photographs collected in 2019 to interpret the longitudinal fracture along the Petermann estuary as well as interpret the Ryder estuary and fractures (Extended Data Table 4).

Climate model. We use the Modèle Atmosphérique Régionale version 3.9 (hereafter referred to as MAR) to qualitatively analyse trends in surface processes from 2010 to 2017 on the Petermann Ice Shelf. MAR is a coupled surface–atmosphere model forced with climate reanalysis data[41] at the lateral boundaries and ocean surface that simulates the surface energy and mass budget in the upper 20 m of the ice surface using a multi-layer approach. Here we use MAR at 7.5 km spatial resolution to assess the liquid water budget.

In MAR, liquid water is present on the ice-shelf when surface melting occurs (there is enough energy to raise the snowpack temperature above 0 °C) or if precipitation falls as rain. Once present, liquid water can percolate into deeper layers of the firn, refreeze or run off the ice surface. MAR includes a simple empirical runoff delay function to account for the delayed release of meltwater as it is routed from the ice surface, accounting for accumulated meltwater over bare ice, excess meltwater that cannot be stored in firn and surface slope[42–44].

We extract MAR outputs at each grid cell over the Petermann Ice Shelf. We mask model outputs using yearly masks of ice-shelf extent from 2010 to 2017 modified from Hill et al.[21] and the approximate location of the grounding line[45]. We compute the fractional area of each grid cell within the boundary to weight the model output values. We spatially integrate model outputs to obtain average estimates of surface melt and snowfall across the entire shelf. We report daily values of surface melt and snow volume.

We use MAR outputs across the Petermann Ice Shelf qualitatively in this analysis. As there are few measurements of in situ melt, errors in these terms are difficult to quantify. MAR generally agrees with in situ and satellite estimates of surface mass balance, meltwater extent and surface air temperature, with ~40% error for point measurements of surface mass balance[46]. MAR version 3.9 includes improvements relative to version 3.5.2 (ref. [46]).

DEM of Antarctica. We use the Reference Model of Antarctica (REMA) to constrain predictions of estuary formation in Antarctica. REMA is an ice-sheet-wide DEM comprised of stereophotogrammetric DEMs created using sub-metre resolution satellite imagery collected by the DigitalGlobe constellation from 2007 to 2017[33]. The final REMA mosaic is a 10-year composite representation of Antarctica's topography that is coregistered to satellite altimetry data[33]. We apply a geoid correction using the GL04C geoid[47].

We use the 100 m spatial resolution, continent-wide DEM in our calculation of estuary formation in a warming world. We use the 8 m DEM with an uncertainty <0.1 m (ref. [33]) to calculate estuary formation under current conditions for the Pine Island Ice Shelf.

Ice-shelf elevation change. We use observations of ice-shelf elevation change $\left(\frac{dh}{dT}\right)$ derived from satellite altimetry to constrain predictions of estuary formation in Antarctica. The $\frac{dh}{dT}$ record spans 1994–2012 and was synthesized from multiple platforms[1]. We use the 27 km resolution gridded data product and corresponding uncertainty. This is a coarse-resolution dataset of $\frac{dh}{dT}$ and does not capture change associated with basal channels or surface-river incision.

We constrain $\frac{dh}{dT}$ on the Larsen B Ice Shelf (excluded from the 18-year record above) with the mean thinning rate derived from satellite radar altimetry from 1992 to 2001 (ref. [34]).

Estuary identification. We identify the Petermann estuary during the melt season in DigitalGlobe imagery (Extended Data Table 2) based on three conditions: (1) water is present in the river channel, (2) no ice obstructs the exchange of water between the river and seawater in the fjord and (3) sea ice is present in the fjord and channel (Fig. 1). Sea ice fragments act as tracers indicating flow direction in the estuary. We also identify the estuary in post melt-season imagery (Extended Data Fig. 1). Following the end of seasonal surface melt, the only water source in the river is seawater. We apply condition (1) to images collected in September to identify the presence of seawater in the channel. While condition (3) is infrequently met during the melt season, we interpret post melt-season imagery as additional evidence that flow reversal can occur during the melt season. The Petermann estuary is also characterized by darkening water at the estuary mouth, consistent with the Beer–Lambert law, that can be seen in satellite and aerial images (Fig. 1b,c).

We use this framework to interpret the sparse dataset of the Ryder estuary. Aerial photography collected in 2019 at the shelf edge reveals deep water at the mouth of the river channel (Fig. 2c). We also identify water in the channel after the melt season in 2014 (Extended Data Fig. 4).

Mapping Petermann estuary evolution. We track the development and evolution of the estuary since 2010 by measuring wetted widths of the Petermann estuary at regular intervals upstream from the calving front. We analyse 31 images from the DigitalGlobe constellation (Extended Data Table 2) collected from June through August 2010–2018 that capture the Petermann Ice Shelf calving front and 3–6 km upstream from the calving front. We display all images using a bilinear interpolation and the North Pole Stereographic projection (EPSG:102018). We pan-sharpen all multispectral images before digitizing and display them in true colour (images with four bands: red, band 4; blue, band 3; green, band 2; images with five bands: red, band 5; blue, band 2; green, band 3).

We digitize the calving front, river centerline, distance along the centerline and river width in each image as follows. First, we trace the calving front 250 m to each side of the Petermann river. Second, we digitize the river centerline to 6 km upstream of the calving front, or to the boundary of the satellite image. Third, we calculate wetted widths along the river perpendicular to the digitized centerline. We identify the water where pixels are dark and select the water/ice edge where there is highest contrast between adjacent pixels. Within the first 75 m of the calving front, downstream of a tributary that joins the Petermann estuary ~100 m from the calving front, we measure wetted widths in 25 m increments. Starting 1 km from the calving front, we measure wetted widths at 1 km intervals. We maintain fixed scales of 1:5000, 1:2500 and 1:1000 when digitizing the calving front, the channel centerline/distance upstream and the channel widths, respectively.

We report the range in width measurements for each increment along the Petermann estuary and river. We consider the greatest source of uncertainty in our standardized width-measurement procedure to be the image pixel size, which is 0.5 m for each image that was digitized, resulting in an uncertainty in width of 1 m (0.5 m on each side of the width measurement). Other sources of uncertainty could include image geolocation and error introduced in digitization. Image geolocation is expected to be roughly uniform across each image, so would not contribute substantially to width-measurement uncertainty. We expect error in the digitization procedure that is not due to the pixel size to be small. The range in widths at all locations is greater than this 1 m uncertainty, and the widening signal seen at the estuary is also greater than 1 m (Extended Data Fig. 3). In the estuarine portion of the river, widths range from 11.18 to 60.43 m (Extended Data Table 5), greater than the 1 m uncertainty estimate. Considering all upstream portions of the river together, widths range from 12.76 to 29.28 m (Extended Data Table 5). The smallest range in widths is 3.86 m, at 5 km upstream. The average width in the estuarine portion of the river is 32.50 m, more than 3 m greater than the widest measurement of 29.28 m observed at upstream locations (Extended Data Table 5). We conclude that the widening signal associated with the estuarine portion of the river is probably due to physical processes such as meltwater production and, critically, flow reversal.

Mapping longitudinal fracture propagation. We digitize the fracture along the bottom of the Petermann estuary in four WorldView images collected in July of 2014–2017 (Extended Data Fig. 5 and Table 2) using a fixed scale of 1:2,500. When multiple fractures are visible, we digitize each individually. We calculate the length of each fracture and the entire fracture system.

We also identify fractures at the Petermann and Ryder estuaries from aerial photography, which show dark linear features along the bottom of both channels (Fig. 2b,c).

The Petermann estuary time constraints. We use the Landsat 8 imagery to constrain the number of days that the Petermann river incises. We identify river incision at the calving front if we detect water at the ice-shelf terminus and continuously along the channel at least 2 km upstream. We identify water at the mouth of Petermann river in 15 images in 2014, 14 images in 2015 and 20 images in 2016. We assume that the river incises between consecutive observations. Water is continuously present at the terminus for 57 days in 2014 (24 June to 18 August), for 60 days in 2015 (28 June to 26 August) and for 60 days in 2016 (11 June to 9 August).

Using satellite and airborne data we constrain the number of melt seasons required for the Petermann river to incise to sea level. The calving event in 2012 marks the first time that the present-day mouth of the Petermann river was exposed to open water in the fjord[15]. WorldView imagery reveals that the rift that formed the 2012 calving event intersected the Petermann river in April 2010 (Extended Data Table 2). We use the OIB DEM (Extended Data Table 4) with a geoid correction[48] to identify the elevation of the channel floor. On 20 April 2010 the channel floor was 3.5 m above sea level. By 30 July 2012 the iceberg drifted out into the fjord, exposing the present-day calving front to open water. We first observe seawater atop the Petermann Ice Shelf in a WorldView-1 image collected on 9 September 2013 (Extended Data Fig. 1 and Table 2). We estimate that the Petermann river incised to sea level to establish an estuary in 1–4 melt seasons.

The Petermann river incision rate. On ice shelves, estuaries develop when rivers incise through underlying ice to sea level. We assume that ice-shelf rivers (~10s of metres wide) are not hydrostatically compensated since they are small compared with the ice thickness (~100s of metres) and that the rest of the ice shelf is hydrostatically compensated at all locations.

We describe the elevation of the channel bottom as:

$$h_f = h_i - \frac{dh}{dT}Y - rNY \tag{1}$$

where h_f (m) is the final channel-bottom elevation, h_i (m) is the initial channel-bottom elevation, $\frac{dh}{dT}$ (m yr^{-1}) is ice-shelf elevation change, Y (yr) is elapsed time, r (m d^{-1}) is the channel incision rate and N (d yr^{-1}) is the duration of river incision each year. When $h_f = 0$ the channel bottom has reached sea level. We express the incision rate as:

$$r = \frac{1}{N}\left(\frac{h_i}{Y} - \frac{dh}{dT}\right). \tag{2}$$

We calculate $\frac{dh}{dT}$ from the thickness change rate as:

$$\frac{dh}{dT} = \frac{\rho_w - \rho_i}{\rho_w}\frac{dH}{dT} \tag{3}$$

where $\frac{dH}{dT}$ is the ice-shelf-thickness change rate and ρ_w and ρ_i are the respective densities of seawater (1,024 kg m^{-3}) and ice (917 kg m^{-3}).

We assume a constant $\frac{dH}{dT}$ and a bare ice surface. We assume that the calculated incision rate, r, is constant over the duration of incision, N. We take N to be 59 d yr^{-1}, the average annual duration of river incision from our Landsat 8 analysis. We take $\frac{dH}{dT}$ from Washam et al.[49], who have measured a net -4.4 ± 0.5 m thickness change over 619 days from in situ radar measurements collected ~35 km upstream of the calving front, adjacent to Petermann river and coincident with the basal channel. We use equation (3) to estimate that $\frac{dh}{dT} = -0.27 \pm 0.03$ m yr^{-1}. Given that Y ranges from 1 to 4 years, we estimate that $r = 1$–5.5 cm d^{-1}. This overlaps with the 3–10 cm d^{-1} range measured on glaciers and ice sheets[22]. The 1 cm d^{-1} lower bound falls outside the measured range but may be plausible given the flat topography of ice shelves.

We estimate the uncertainty associated with the measurements used to constrain the other terms by considering the upper and lower bounds on each; N ranges from 57 to 60 days, h_i ranges from 3.4 to 3.6 m and $\frac{dh}{dT}$ ranges from -0.3 to -0.24 m yr^{-1}. Taking these ranges into account, we estimate that the bounds of r with uncertainty are 1 ± 0.15 cm d^{-1} and 5.5 ± 0.35 cm d^{-1}.

Nansen river incision rate. We calculate the incision rate of the Nansen river (i) using observations from Bell et al.[8] and the following equation from Fountain and Walder[50]:

$$i = \frac{1}{2}\left(\frac{\pi}{2n}\right)^{\frac{3}{8}}\frac{\rho_w}{\rho_i}\frac{g}{h_{iw}}S^{\frac{19}{16}}Q^{\frac{5}{8}} \tag{4}$$

where $n = 0.01$ s m$^{-1/3}$, ρ_w and ρ_i are the respective densities of water (1,000 kg m^{-3}) and ice (917 kg m^{-3}), g is the gravitational constant (9.81 m s^{-2}), $h_{iw} = 3.35 \times 10^5$ J kg^{-1} is the latent heat of fusion, S is the slope of the channel bottom and Q is discharge.

The equation assumes that the channel bottom is smooth, the channel does not widen and all energy dissipated by water flow goes into melting. We take $S = 0.0019$ and the most conservative value of $Q = 80$ m^3 s^{-1} from Bell et al.[8]. We calculate i to be 7.2 cm d^{-1}, within the range of observed river and stream incision rates[22].

Most river discharge observations fall below 1 m^3 s^{-1} and the maximum discharge rate observed from a single river/stream on glaciers and ice sheets ranges from 0.016 to 26.73 m^3 s^{-1} (ref. [22]). Thus, we consider that 80 m^3 s^{-1} is an overestimate of Q and that our derived incision rate of 7.2 cm d^{-1} is high for the Nansen river.

Modelling estuary formation on ice shelves under current conditions. We use a modified equation (2) to calculate Y (yr), assuming current conditions, on the Petermann, Nansen, Pine Island and Larsen B ice shelves (Fig. 4a), where surface rivers[7–9,16,29] and/or basal channels[9,13,14,51] have been observed. We present our results as a function of incision rate (Fig. 4a). We favour the 3 cm d^{-1} reported incision rate[22], as it falls within the range calculated for the Petermann river. We use melt-season duration, a, as a proxy for N, as no studies have quantified the persistence of ice-shelf rivers broadly, and assume that the river incises continuously. Constraints are listed in Extended Data Table 1. We estimate uncertainty by calculating the range reported with these constraints.

Although we previously estimated that the Petermann river required between one and four years to incise to sea level, we include Petermann in these calculations for comparison. We find that the Petermann estuary would have formed in 1.7 years, consistent with our observations. Considering uncertainty, this estimate ranges from 1.62 to 1.85 years.

We estimate that the Nansen river could form an estuary in 29 years. Using observations from Bell et al.[8], we calculate that Nansen waterfall was observed for 18 days on average. The uncertainty in the Nansen waterfall duration is 9.4 days[8]. There is no uncertainty reported for the channel elevation. However, the elevation was measured with OIB's Airborne Topographic Mapper[8], which has a vertical accuracy of 0.1 m (ref. [52]). We calculate that Y ranges from 17.9 to 70.9 years.

We estimate that an estuary could develop on the Pine Island Ice Shelf in 40 years. We measure h_i from the 8 m REMA DEM[33] with a GL04C geoid correction[47]. We extract an elevation profile orthogonal to ice flow by employing a similar procedure used to measure widths along the Petermann river. We sample the DEM at 8 m intervals along the profile and take the minimum elevation (Extended Data Table 1). We calculate that Y ranges from 38.0 to 42.4 years.

We estimate that an estuary may have developed on the Larsen B Ice Shelf in 8 years. Here we calculate h_i using the minimum ice-shelf-thickness measurement of 179 m from Rack and Rott[32] (Extended Data Table 1) and equation (3). We calculate N by digitizing melt-days data from Scambos et al.[31] (Extended Data Table 1) using WebPlotDigitizer (https://automeris.io/WebPlotDigitizer) and calculate the standard error to be 3.65 days. We calculate that Y ranges from 7.3 to 9.3 years.

Modelling estuary formation on ice shelves in a warming world. We use a modified equation (2) to calculate N, number of days of river incision required to form an estuary on Antarctica's ice shelves in 30 years. We again redefine N as melt-season duration. We use Pitcher and Smith's[22] lowest estimate of r, 3 cm d^{-1}. We take h_i from the geoid-corrected REMA DEM[33,47], down-sampled to 27 km to match the resolution of the $\frac{dh}{dT}$ data[1]. We apply modified equation (2) to each grid cell.

We calculate the range in N due to uncertainty in $\frac{dh}{dT}$ (ref. [1]) and h_i (ref. [33]). For 40% of grid cells, $0 < N < 1$ day and for 30% $1 < N < 2$ days. We also report sensitivity to r, which we demonstrated earlier is high. Taking $1 < r < 10$ cm d^{-1} we find that $10 < N < 20$ days in 56% of grid cells.

We present a range of scenarios for ice-shelf estuary formation given available observations. We assume that rivers incise at a constant rate each day of the melt season, an oversimplification that does not account for diurnal variability in the river hydrograph[44] that modulates incision rates[50]. We do not account for other surface hydrologic processes, such as water storage and transport through firn or a bare ice weathering crust[53,54], which modulate the delivery of surface meltwater to rivers.

Data availability

Except for DigitalGlobe constellation data, all datasets used in this analysis are freely available. DigitalGlobe satellite imagery was provided by the PGC under National Science Foundation grant 1644869 and is available from the PGC upon request with eligible active research awards. Imagery-derived river widths and fracture length developed in this analysis are available at http://wonder.ldeo.columbia.edu/data/publicationData/Boghosian/Estuary/, along with MAR data used. Landsat data are available at https://earthexplorer.usgs.gov and the Landsat Image Mosaic of Antarctica is available at https://nimbus.cr.usgs.gov/landing/. OIB data are provided by the National Snow and Ice Data Center at https://nsidc.org/. The 1978 orthophotos are provided by the National Oceanic and Atmospheric Administration National Centers for Environmental Information at https://www.nodc.noaa.gov/archive/arc0088/0145405/1.1/data/0-data/G150AERODEM/Orthorectified/. Ice-shelf elevation data are available at https://sealevel.nasa.gov/data/dataset/?identifier=SLCP_ice_shelf_dhdt_v1_1. REMA data are available through the PGC at https://www.pgc.umn.edu/data/rema/.

Code availability

This analysis does not depend on specific code. All results can be reproduced through the equations and procedures outlined in the Methods section of this manuscript.

References

39. Dominguez, R. *IceBridge DMS L1B Geolocated and Orthorectified Images, Version 1* (NASA National Snow and Ice Data Center Distributed Active Archive Center, 2019); https://doi.org/10.5067/OZ6VNOPMPRJ0
40. Arvesen, J. C. & Dotson, R. C. Photogrammetric processing of IceBridge DMS imagery into high-resolution digital surface models (DEM and visible overlay). In: *AGU Fall Meeting 2014* C21D–03 (AGU, 2014).
41. Dee, D. et al. The ERA-Interim Reanalysis: configuration and performance of the data assimilation system. *Q. J. R. Meteorol. Soc.* **137**, 553–597 (2011).
42. Lefebre, F., Gallée, H., van Ypersele, J.-P. & Greuell, W. Modeling of snow and ice melt at ETH Camp (West Greenland): a study of surface albedo. *J. Geophys. Res. Atmos.* **108**, 4231 (2003).
43. Smith, L. C. et al. Direct measurements of meltwater runoff on the Greenland ice sheet surface. *Proc. Natl Acad. Sci. USA* **114**, E10622–E10631 (2017).
44. Zuo, Z. & Oerlemans, J. Modelling albedo and specific balance of the Greenland ice sheet: calculations for the Søndre Strømfjord transect. *J. Glaciol.* **42**, 305–317 (1996).
45. Forster, R. R. et al. Extensive liquid meltwater storage in firn within the Greenland ice sheet. *Nat. Geosci.* **7**, 95–98 (2013).
46. Fettweis, X. et al. Reconstructions of the 1900–2015 Greenland ice sheet surface mass balance using the regional climate MAR model. *Cryosphere* **11**, 1015–1033 (2017).
47. Förste, C. et al. The GeoForschungsZentrum Potsdam/Groupe de Recherche de Gèodésie Spatiale satellite-only and combined gravity field models: EIGEN-GL04S1 and EIGEN-GL04C. *J. Geod.* **82**, 331–346 (2008).
48. Morlighem, M. et al. BedMachine v3: complete bed topography and ocean bathymetry mapping of Greenland from multibeam echo sounding combined with mass conservation. *Geophys. Res. Lett.* **44**, 11051–11061 (2017).
49. Washam, P., Nicholls, K. W., Münchow, A. & Padman, L. Summer surface melt thins Petermann Gletscher Ice Shelf by enhancing channelized basal melt. *J. Glaciol.* **65**, 662–674 (2019).
50. Fountain, A. G. & Walder, J. S. Water flow through temperate glaciers. *Rev. Geophys.* **36**, 299–328 (1998).
51. Vaughan, D. G. et al. Subglacial melt channels and fracture in the floating part of Pine Island Glacier, Antarctica. *J. Geophys. Res. Earth Surf.* **117**, F03012 (2012).
52. Martin, C. F. et al. *Airborne Topographic Mapper Calibration Procedures and Accuracy Assessment* Report No. NASA/TM–2012-215891 (NASA, 2012).
53. Irvine-Fynn, T. D. L., Hodson, A. J., Moorman, B. J., Vatne, G. & Hubbard, A. L. Polythermal glacier hydrology: a review. *Rev. Geophys.* **49**, RG4002 (2011).
54. Cooper, M. G. et al. Meltwater storage in low-density near-surface bare ice in the Greenland ice sheet ablation zone. *Cryosphere* **12**, 955–970 (2018).

Author contributions

A.L.B. contributed to conceptualization and investigation of the project, methodology, data analysis and visualization, and wrote the manuscript. All authors contributed to the manuscript. L.H.P. contributed to conceptualization and investigation of the project, methodology and data analysis, and provided resources. L.C.S. contributed to the conceptualization and investigation of the project. E.K. contributed to data analysis and visualization. P.M.A. and M.T. contributed data resources and to data analysis. R.E.B. contributed to conceptualization and investigation of the project.

Competing interests

The authors declare no competing interests.

Additional information

Extended data is available for this paper at https://doi.org/10.1038/s41561-021-00837-7.

Supplementary information The online version contains supplementary material available at https://doi.org/10.1038/s41561-021-00837-7.

Correspondence and requests for materials should be addressed to Alexandra L. Boghosian.

Peer review information Primary Handling Editor: Thomas Richardson, in collaboration with the *Nature Geoscience* team. *Nature Geoscience* thanks Knut Christianson and the other, anonymous, reviewer(s) for their contribution to the peer review of this work.

Reprints and permissions information is available at www.nature.com/reprints.
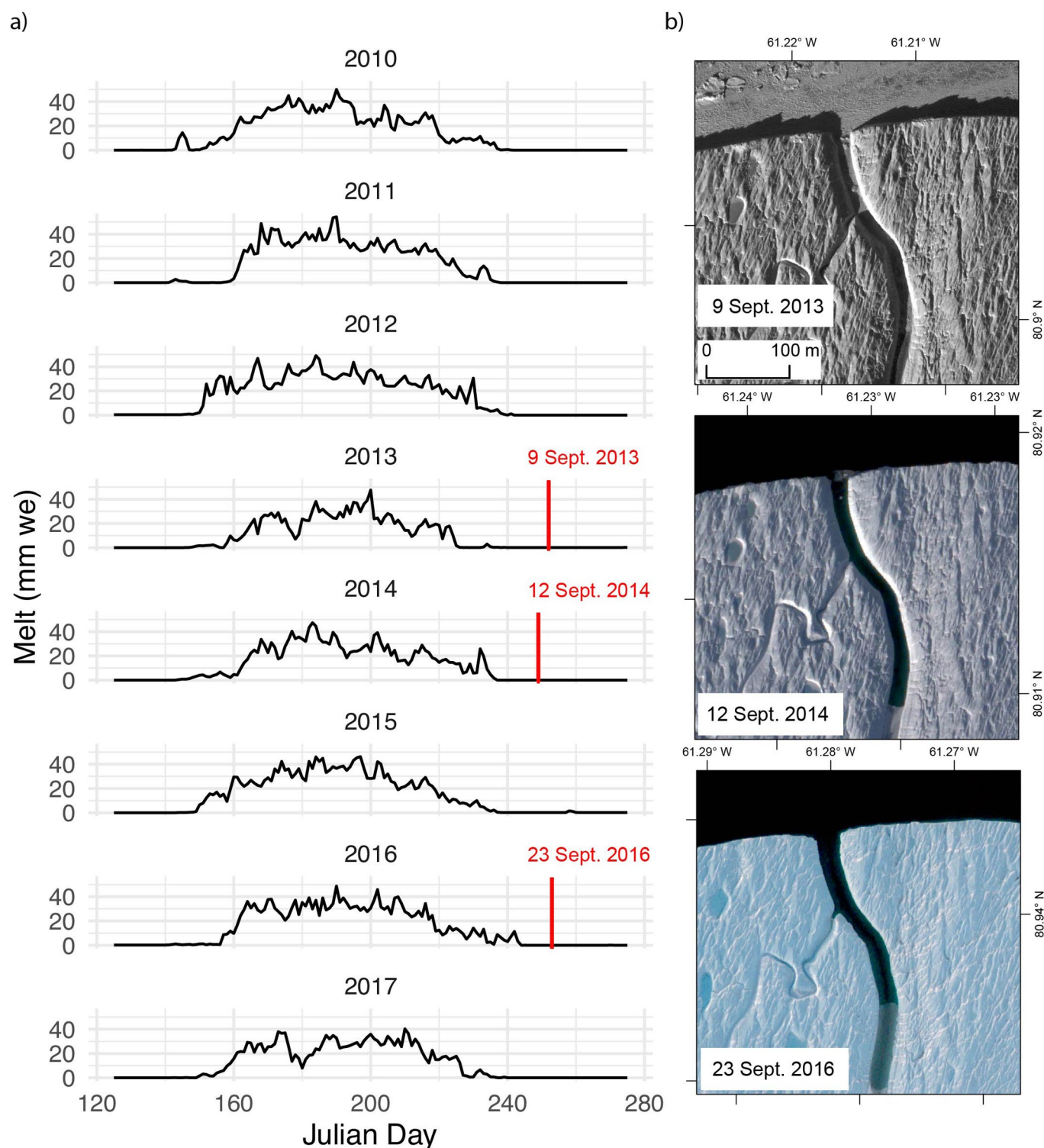
Extended Data Fig. 1 | Ocean water atop the Petermann Ice Shelf after the melt season. a Modèle Atmosphérique Regional v. 3.9 (MAR) average daily ice-surface melt averaged across the Petermann Ice Shelf from 2010 to 2017. The red dotted lines show earliest indication of seawater in the channel after the melt season as identified in high resolution WorldView-1 and WorldView-2 satellite imagery (Extended Data Table 2). **b** The first evidence of water atop the ice shelf was collected by WorldView-1 in 2013 (top). Note that break in the shadow cast by the ice-shelf terminus at the Petermann river channel confirms a direct connection between the ice shelf and the ocean. Multispectral WorldView-2 images collected in 2014 (middle) and 2016 (bottom) show water in the channel directly connected to the ocean and an absence of surface meltwater elsewhere on the ice shelf. Credit: b, (2013, 2014, 2016) DigitalGlobe, Inc.
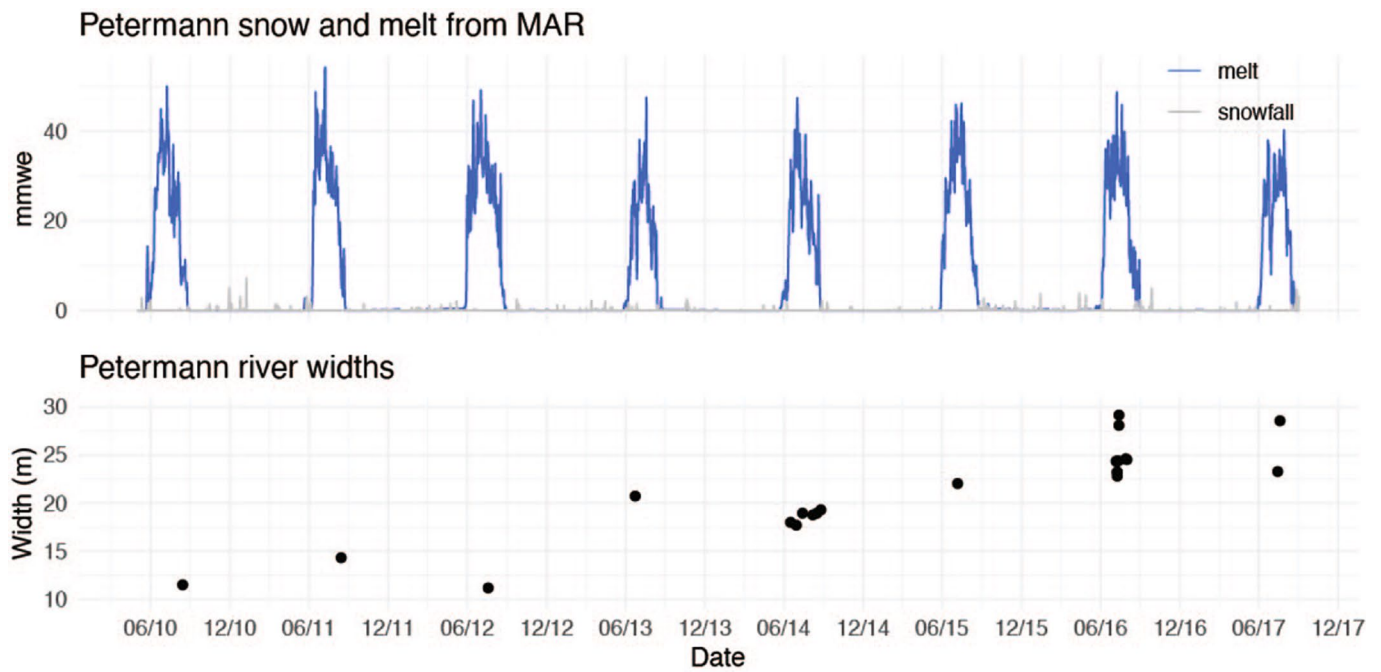
Extended Data Fig. 2 | Modelled melt and snowfall on Petermann Ice Shelf. Top: MAR simulation of daily surface melt (blue) and snowfall (gray) averaged across the Petermann Ice Shelf from 2010 to 2017. Melt and snowfall are reported in millimeters water equivalent (mmwe), which is used to represent snow or ice mass in terms of its equivalent water volume. Bottom: estuary wetted widths measured at 25 m from calving front as in Extended Data Fig. 3 from 2010 to 2017. This demonstrates the lack of correlation between estuary widening and surface runoff.
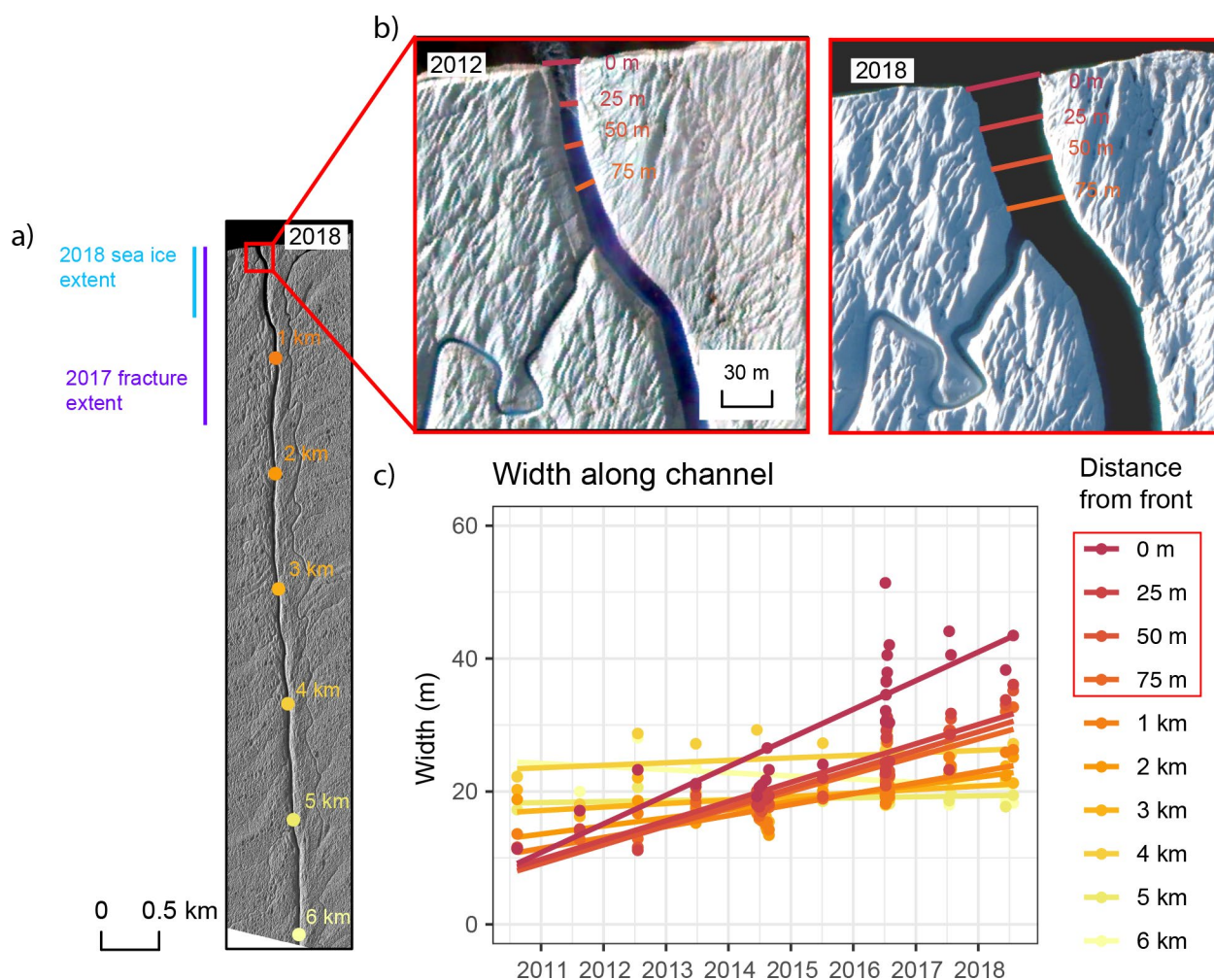
Extended Data Fig. 3 | Evidence for change at the mouth of the estuary. a Location of wetted width measurements at 1 km increments along the Petermann river set against pan-chromatic WorldView-2 image (30 August 2018). Blue line denotes the maximum extent of sea ice found in the channel, (24 July 2018). Purple line denotes the maximum extent of the longitudinal fracture (25 July 2017). Red box shows the location of Extended Data Fig. 3b. **b** The mouth of the Petermann estuary widened from 2012 (left) to 2018 (right). Left panel: 2012 image with river widths shown as colored lines at 25 m increments from the ice-shelf front (QuickBird image July 19th). Right panel: 2018 image with river widths at 25m increments as in left panel. The estuary is approximately three times wider in 2018. **c** Wetted width measurements along channel from 2010 to 2018. The channel widens at the mouth of the estuary and within 2 km from the ice-shelf front. Width measurements (points) and trendlines are colored by locations marked in Extended Data Fig. 3a,b. Fracture growth and flow reversal evidence are coincident with this widening as shown in **a**. Credit: a,b (left): (2012, 2018) DigitalGlobe, Inc.
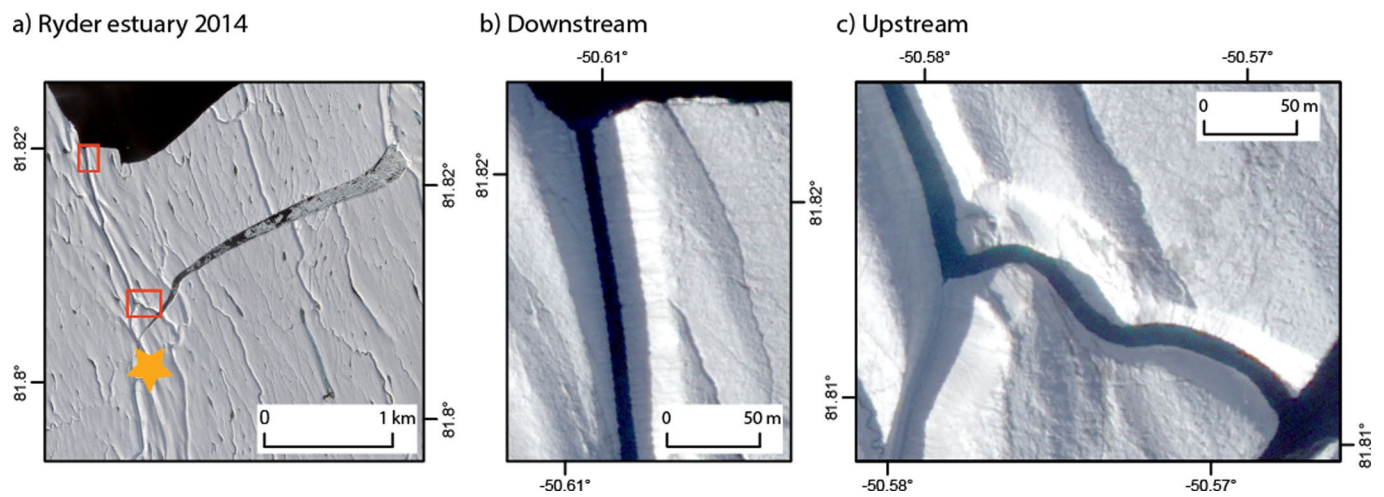
Extended Data Fig. 4 | Additional evidence for the Ryder Ice Shelf estuary. (**a**) The Ryder estuary in a WorldView-2 image collected on 25 August 2014. Red boxes mark the location of (b) and (c), and gold star marks the approximate location of the 2019 estuary (Fig. 2c). (**b**) Detailed image of the downstream portion of the estuary shows water in the channel directly connected to the ocean and an absence of surface meltwater elsewhere on the ice shelf. (**c**) Detailed image of the upstream portion of the estuary shows water in the channel directly connected to ocean water in the rift and an absence of surface meltwater elsewhere on the ice shelf. Credit: (2014) DigitalGlobe, Inc.
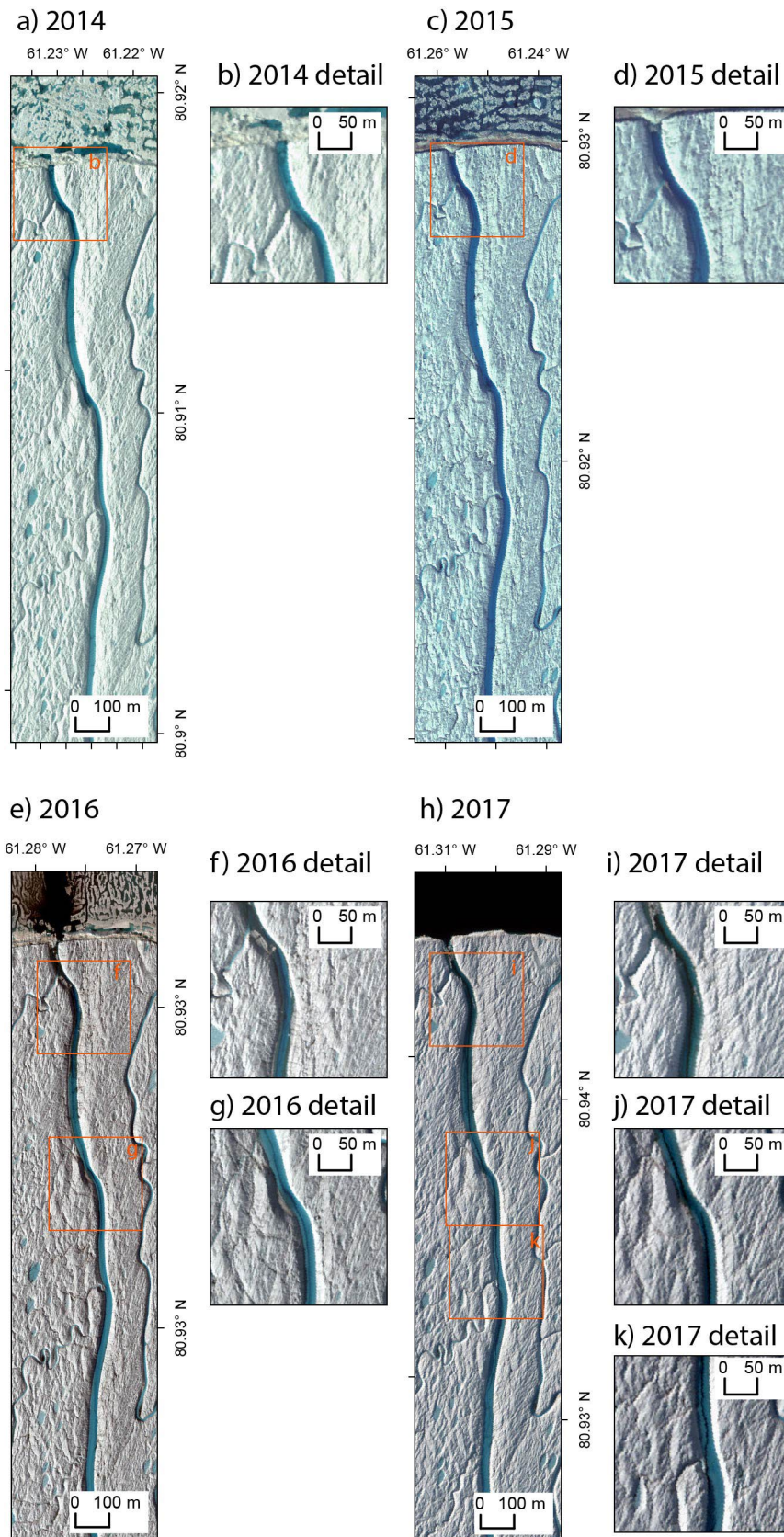
Extended Data Fig. 5 | Detail of longitudinal fractures at the Petermann estuary. WorldView imagery at the Petermann estuary from which fractures were digitized (Fig. 2a). Red boxes show location of detail views. Fractures are identified as dark linear features along the bottom of the channel. Images collected on 14 July 2014; 17 July 2015; 15 July 2016; and 25 July 2017. Credit: (2014, 2015, 2016, 2017) DigitalGlobe Inc.

Extended Data Table 1 | Constrains used in estuary calculations

Petermann Ice Shelf	Value	Uncertainty	Source
River duration (N)	59 d yr^{-1}	57- 60 d yr^{-1}	Landsat 8 imagery
Elevation change rate ($\frac{dh}{dT}$)	-0.27 m yr^{-1}	± 0.03 m yr^{-1}	Calculated from Washam et al.[1]
Initial channel elevation (h_i)	3.5 m	± 0.1 m	OIB DMS DEM[2,3]
Nansen Ice Shelf			
Waterfall duration (N)	18 d yr^{-1}	± 9.4 d yr^{-1}	Calculated and taken from Bell et al.[4]
Elevation change rate ($\frac{dh}{dT}$)	-0.018 m yr^{-1}	± 0.049 m yr^{-1}	Paolo et al.[5]
Initial channel elevation (h_i)	16 m	± 0.1 m	Bell et al.[4], OIB ATM[6]
Larsen B Ice Shelf			
Melt season duration (a)	55 d yr^{-1}	± 3.65 d yr^{-1}	Calculated from Scambos et al.[7]
Elevation change rate ($\frac{dh}{dT}$)	-0.17 m yr^{-1}	±0.11 m yr^{-1}	Shepherd et al. [8]
Initial channel elevation (h_i)	14.86 m	NA	Calculated from Rack and Rott[9]
Pine Island Ice Shelf			
Melt season duration (a)	37 d yr^{-1}	NA	Trusel et al.[10,11]
Elevation change rate ($\frac{dh}{dT}$)	-0.1480 m yr^{-1}	± 0.062 m yr^{-1}	Paolo et al.[5]
Initial channel elevation (h_i)	50.4 m	± 0.1 m	REMA

Constraints used in the estuary formation and timing calculations shown in Fig. 4a

Extended Data Table 2 | DigitalGlobe images used

Date	Sensor	ID	Ice Shelf	Purpose	
20100605	QB02	20100605212925	PIS	RF	
20100814	WV02	20100814001457	PIS	RW	
20110815	WV02	20110815211856	PIS	RW	RF
20120719	QB02	20120719222250	PIS	RW	RF
20130623	WV02	20130623001130	PIS	RW	
20130907	WV01	20130907180843	PIS	EI	
20140617	WV02	20140617213111	PIS	RW	
20140630	WV02	20140630201224	PIS	RW	
20140714	WV02	20140714195621	PIS	RW	
20140714	WV02	20140714195554	PIS	RW	LF
20140716	WV02	20140716015653	PIS	RW	
20140807	WV02	20140807215011	PIS	RW	
20140816	WV02	20140816225825	PIS	RW	
20140824	WV01	20140824190017	PIS		
20140825	WV02	20140825190825	RIS	EI	
20140825	WV02	20140825172840	PIS	RW	
20140912	WV02	20140912180509	PIS	EI	
20150707	WV02	20150707193617	PIS	RW	
20150710	WV02	20150710174621	PIS	LF	
20160707	WV02	20160707212152	PIS	RW	
20160709	WV01	20160709223452	PIS	RW	
20160709	WV01	20160709223423	PIS	RW	
20160710	WV01	20160710014141	PIS	RW	
20160713	WV02	20160713210049	PIS	RW	
20160713	WV02	20160713174223	PIS	RW	
20160715	WV03	20160715184944	PIS	LF	
20160717	WV02	20160717215216	PIS	RW	
20160717	WV02	20160717183424	PIS	RW	
20160729	WV01	20160729213646	PIS	RW	
20160731	WV01	20160731205334	PIS	RW	
20160923	WV02	20160923200448	PIS	EI	
20170707	GE01	20170707170717	PIS	RW	
20170714	WV01	20170714011019	PIS	RW	
20170720	WV01	20170720020502	PIS	RW	
20170725	WV02	20170725222506	PIS	RW	LF
20180611	WV02	20180611204247	PIS	RW	
20180724	WV02	20180724192143	PIS	RW	EI
20180726	WV01	20180726015346	PIS	RW	EI
20180831	WV03	20180831214021	PIS	RW	

Complete list of DigitalGlobe images analyzed of the Petermann Ice Shelf (PIS) and Ryder Ice Shelf (RIS). Purpose is included with categories: river widths measured (RW), rift forming 2012 calving event (RF), estuary identification (EI), and longitudinal fractures measured (LF)

Extended Data Table 3 | Landsat images used

Landsat Scene	Purpose
LE07_L1TP_044001_19990707_20170218_01_T1	RC
LE07_L1TP_030248_20080713_20161228_01_T1	RC
LE07_L1TP_033247_20100708_20161213_01_T1	RC
LC08_L1TP_042001_20140624_20170421_01_T1	RD
LC08_L1TP_031248_20140627_20170304_01_T1	RD
LC08_L1TP_045001_20140629_20170304_01_T1	RD
LC08_L1TP_043001_20140701_20170304_01_T1	RD
LC08_L1TP_064243_20140704_20170421_01_T1	RD
LC08_L1TP_030248_20140706_20170305_01_T1	RD
LC08_L1TP_045001_20140715_20170304_01_T1	RD
LC08_L1TP_061243_20140731_20170420_01_T1	RD
LC08_L1TP_052244_20140801_20170420_01_T1	RC
LC08_L1TP_030248_20140807_20170304_01_T1	RD
LC08_L1TP_044001_20140809_20170304_01_T1	RD
LC08_L1TP_058244_20140811_20170420_01_T1	RD
LC08_L1TP_065243_20140812_20170420_01_T1	RD
LC08_L1TP_045001_20140816_20170304_01_T1	RD
LC08_L1TP_043001_20140818_20170304_01_T1	RD
LC08_L1TP_044001_20140825_20170303_01_T1	RD
LC08_L1TP_033248_20150628_20170407_01_T1	RD
LC08_L1TP_034248_20150705_20170407_01_T1	RD
LC08_L1TP_030248_20150709_20170226_01_T1	RD
LC08_L1TP_044001_20150711_20170227_01_T1	RD
LC08_L1TP_035248_20150712_20170407_01_T1	RD
LC08_L1TP_042001_20150713_20170226_01_T1	RD
LC08_L1TP_033248_20150714_20170407_01_T1	RD
LC08_L1TP_040001_20150715_20170226_01_T1	RD
LC08_L1TP_040001_20150731_20170226_01_T1	RD
LC08_L1TP_031248_20150801_20170226_01_T1	RD
LC08_L1TP_038002_20150802_20170226_01_T1	RD
LC08_L1TP_044001_20150812_20170226_01_T1	RD
LC08_L1TP_035248_20150813_20170406_01_T1	RD
LC08_L1TP_040001_20150816_20170226_01_T1	RD
LC08_L1TP_044001_20160611_20170223_01_T1	RD
LC08_L1TP_035248_20160612_20170324_01_T1	RD
LC08_L1TP_063243_20160616_20170323_01_T1	RD
LC08_L1TP_038002_20160617_20170222_01_T1	RD
LC08_L1TP_061243_20160618_20170323_01_T1	RD

Landsat Scene	Purpose
LC08_L1TP_062243_20160625_20170323_01_T1	RD
LC08_L1TP_064243_20160709_20170323_01_T1	RD
LC08_L1TP_055244_20160710_20170323_01_T1	RD
LC08_L1TP_062243_20160711_20170323_01_T1	RD
LC08_L1TP_044001_20160713_20170222_01_T1	RD
LC08_L1TP_035248_20160714_20170323_01_T1	RD
LC08_L1TP_042001_20160715_20170222_01_T1	RD
LC08_L1TP_040001_20160717_20170222_01_T1	RD
LC08_L1TP_063243_20160718_20170323_01_T1	RD
LC08_L1TP_038002_20160719_20170221_01_T1	RD
LC08_L1TP_041001_20160724_20170222_01_T1	RD
LC08_L1TP_043001_20160807_20170222_01_T1	RD
LC08_L1TP_041001_20160809_20170222_01_T1	RD
LC08_L1TP_041001_20160825_20170221_01_T1	RD
LC08_L1TP_032248_20160826_20170223_01_T1	RD

Complete list of Landsat 8 OLI and Landsat 7 ETM+ scenes analyzed. Purpose is included with categories: rectilinear calving (RC), and river duration (RD)

Extended Data Table 4 | Aerial images, DEMs and field photographs used

Aerial Imagery and DEM	Date	Type	Source/Credit
IODIM3_20100420_181506_10857_ORTHO.jpg	4/20/2010	orthophoto	OIB
IODEM3_20100420_181504_10856_DEM.tif	4/20/2010	DEM	OIB
g150_1978_utm20.jp2	7/3/1978	orthophoto	Korsgaard et al.[12]
Petermann Aerial 1	7/15/2019	Field Photography	Roger Fishman
Petermann Aerial 2	7/27/2019	Field Photography	Matthias Vogt
Ryder Aerial 3	10/13/2019	Field Photography	Josh Willis
Ryder Aerial 4	11/8/2019	Field Photography	Josh Willis

Complete list of aerial images, derived DEMs and field photographs used

Extended Data Table 5 | Wetted width statistics

Increment	Minimum (m)	Maximum (m)	Range (m)
0 m	11.38	60.43	49.05
25 m	11.18	39.99	28.81
50 m	11.33	38.35	27.03
75 m	11.64	36.82	25.18
1000 km	12.76	27.81	15.06
2000 km	13.44	25.31	11.87
3000 km	14.17	23.81	9.64
4000 km	18.08	29.28	11.20
5000 km	17.24	21.10	3.86
6000 km	16.69	28.07	11.37

Range in channel wetted width measurements